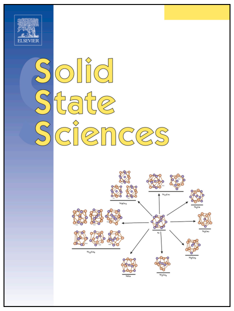

Synthesis and characterization of perovskite-type $La_{1-y}Ca_yMn_{1-x}B''_xO_{3\pm\delta}$ nanomaterials (B’’ = Ni, Fe; x = 0.2, 0.5; y = 0.4, 0.25)

Daniela Franke, Dmytro Trots, Leonid Vasylechko, Vladimir Vashook, Ulrich Guth

PII: S1293-2558(17)30672-6
DOI: 10.1016/j.solidstatesciences.2017.12.008
Reference: SSSCIE 5610

To appear in: *Solid State Sciences*

Received Date: 9 July 2017
Revised Date: 10 December 2017
Accepted Date: 19 December 2017

Please cite this article as: D. Franke, D. Trots, L. Vasylechko, V. Vashook, U. Guth, Synthesis and characterization of perovskite-type $La_{1-y}Ca_yMn_{1-x}B''_xO_{3\pm\delta}$ nanomaterials (B’’ = Ni, Fe; x = 0.2, 0.5; y = 0.4, 0.25), *Solid State Sciences* (2018), doi: 10.1016/j.solidstatesciences.2017.12.008.

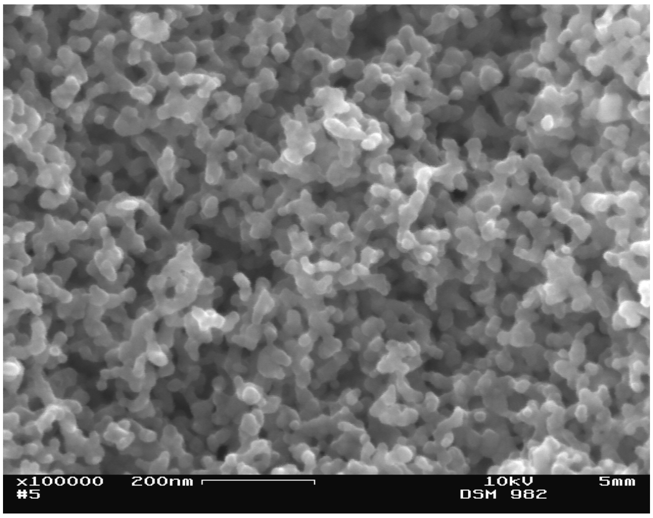
x100000
200nm
10kV
5mm
#5
DSM 982

Synthesis and characterization of perovskite-type $La_{1-y}Ca_yMn_{1-x}B''_xO_{3\pm\delta}$ nanomaterials (B'' = Ni, Fe; x = 0.2, 0.5; y = 0.4, 0.25)

Daniela Franke[a*,1], Dmytro Trots[b,2], Leonid Vasylechko[c], Vladimir Vashook[a], Ulrich Guth[a,d]

a Institute of Physical Chemistry and Electrochemistry, Technische Universität Dresden, 01062 Dresden, Germany
b HASYLAB at DESY, Notkestr. 85, 22607 Hamburg, Germany
c Lviv Polytechnic National University, 12 Bandera St., 79013 Lviv, Ukraine
d Kurt Schwabe Institute for Measurement and Sensor Technology Meinsberg, Kurt-Schwabe-Str. 4, 04736 Waldheim, Germany
1 Current address: Technische Universität Dresden, Electrical and Computer Engineering Department, Solid-State Electronics Laboratory, 01062 Dresden, Germany
2 Current address: Carl Zeiss SMS, Carl-Zeiss-Promenade 10, 07745 Jena, Germany

*Corresponding author: daniela.franke@tu-dresden.de

Abstract

Perovskite-type nanomaterials of the compositions $La_{1-y}Ca_yMn_{1-x}B''_xO_{3\pm\delta}$ with B'' = Ni, Fe; x = 0.2, 0.5 and y = 0.4, 0.25 were prepared using two different preparation routes (synthesis by precipitation and the PVA/sucrose method) at 500°C to 700°C. The calcined products of the syntheses were characterized by X-ray diffraction (XRD), scanning electron microscopy (SEM), energy-dispersive X-ray spectroscopy (EDX) and physisorption measurements. The materials from the PVA/sucrose method contain particles with diameters from 33 nm to 48 nm, generate specific surface areas up to 33 m^2/g and form pure compared to 45 nm to 93 nm and up to 18 m^2/g from precipitation method which contain a significant amount of sodium ions. The agglomeration process was analyzed for one nanomaterial (B'' = Fe, x = 0.2, y = 0.4) from the PVA/sucrose method using temperature dependent XRD showing only a slight growth (4.3%) of nanoparticles at 600°C. The materials from the the PVA/sucrose method turned out to be more suitable as electrode materials in electrochemical applications (SOFC, sensors) because of smaller particle sizes, higher specific surface areas and purity.

Keywords: perovskite-type manganites; PVA/sucrose method; precipitation; nanostructured materials.

1 Introduction

Multiple publications show several methods for the preparation of multi-element perovskite-type nanomaterials using different methods of wet chemistry. A variety of reaction principles have been proven to be successful, such as freeze-drying [1], hydrothermal and solvothermal synthesis [2-6], flame-pyrolysis of a precursor solution [7], microemulsion with reverse micelles [8,9], activated-carbon route [10,11], PVA/sucrose method and miscellaneous precipitation methods. Among the precipitation syntheses, Siemons et al. showed the preparation of $CaTiO_3$, $SrTiO_3$ and $LaMnO_3$ by polyol method [12]. Vasseur et al. prepared nano-sized $La_{0.75}Sr_{0.25}MnO_3$ by Pechini method [13]. Both methods are based on chelate formation of reactants to create spacing between crystal nuclei.

Regarding the PVA/sucrose method Panda and coworkers described the formation of a branched polymer network based on polyvinyl alcohol (PVA) and sucrose [14]. The simultaneous evaporation of an aqueous metal salt solution leads to a long range dispersion of ions or crystal nuclei in the polymer matrix preventing the agglomeration of nanoparticles during calcination. Pramanik showed the preparation of perovskites ($GdFeO_3$, $SmFeO_3$, $LaAlO_3$, $NdGaO_3$, PZT/PLZT) and spinels ($MeFe_2O_4$ with Me = Ni, Co, Zn, Mg) with particle sizes between 30 nm and 300 nm using only a PVA matrix [15]. Panda and coworkers used the above-mentioned PVA/sucrose matrix to prepare $SrBi_2Ta_2O_9$ with particle sizes of 35 nm [14]. Wohlrab et al. prepared alkaline niobates $MNbO_3$ (with M = Li, Na, K) with particle sizes between 31 nm and 68 nm [11]. The mixtures differed in the molar ratio of PVA/sucrose/metal salt.

Recently, perovskite-type nanomaterials showed improved properties for applications as electrode materials in potentiometric sensors [16-20] and SOFC [21, 22] as well as better processibility when preparing membranes for catalysis because sintering of the nanomaterials takes place at lower temperatures [23]. In our previous works, the bulkmaterials $La_{0.6}Ca_{0.4}Mn_{0.8}Ni_{0.2}O_{3\pm\delta}$ (LCMN82), $La_{0.6}Ca_{0.4}Mn_{0.8}Fe_{0.2}O_{3\pm\delta}$ (LCMF82) and $La_{0.75}Ca_{0.25}Mn_{0.5}Fe_{0.5}O_{3\pm\delta}$ (LCMF55) showed enhanced NO sensitivity in potentiometric and impedance setups [24, 25]. For this work, nanomaterials of these compositions were prepared by a simple precipitation method using sodium hydroxide solution as the precipitating agent and by PVA/sucrose method. The results of this work regarding particle sizes/specific surface areas, purity and agglomeration at intermediate temperatures provide the basis for further electrochemical measurements (mixed potential sensors, SOFC) which will be published later. The appropriate nanomaterials from this work will be chosen as electrode materials for these purposes.

2 Material and methods

2.1 Synthesis by precipitation

A slight excess of 3 M sodium hydroxide solution was added to a stoichiometric solution of lanthanum nitrate hexahydrate, calcium nitrate tetrahydrate, manganese acetate tetrahydrate and nickel nitrate hexahydrate / iron(III) nitrate nonahydrate. The suspension of hydroxides was stirred for 12 hours while Mn^{2+} ions were oxidized to Mn^{4+} ions. After filtration the amorphous mixture of hydroxide-oxides was dried at 70°C for 12 hours. Samples were calcined at 500°C to 700°C for 3 to 5 hours.

2.2 Synthesis by PVA/sucrose method

Two ratios of PVA/sucrose/metal ions were chosen to prepare LCMN82, LCMF82 and LCMF55 nanomaterials. Mixture 1 contained PVA : sucrose : metal ions with the molar ratio 3 : 30 : 1 as in [11] and mixture 2 contained PVA : sucrose : metal ions with the molar ratio 1 : 27 : 5. PVA, sucrose, the above-mentioned metal salts and 200 ml of deionized water were stirred in a covered beaker on a hot plate at 300°C until all compounds were dissolved. Then, the beaker was uncovered and the temperature was slowly reduced to 200°C while the water evaporated from the solution and a caramel-like residuum occurred. This residuum was transferred to a ceramic dish which was then placed in a furnace and heated at 250°C for 30 min. Depending on the initial mixture a porous solid black or porous fluffy brown precursor was formed and calcined in a second temperature step at 500°C or 600°C for 30 min to 3 hours. For comparison, PVAs with different molecular weights were chosen, one containing 60000 monomer units and one containing 145000 monomer units.

2.3 Characterization

X-ray diffraction (XRD) of the powder samples was carried out in a Huber Image Plate camera G670 (Cu$K_{\alpha1}$ radiation, 3° < 2θ < 100°, step width 0.005° of 2θ). The diffractograms were analyzed with full-profile Rietveld refinement using the Windows version of the Crystal Structure Determination program package (WinCSD) [26]. The calculations included the refinement of lattice parameters, positional and displacement parameters of atoms, scaling factor, absorption, zero shift, background and Bragg-peak profile parameters.

In situ crystal structure investigations between room temperature and 1173 K using the LCMF82 bulkmaterial and the LCMF82 nanomaterial from PVA/sucrose method (mix 2, PVA 145000; calcination: 600 °C for 3 hours) were carried out with high-resolution powder diffraction applying synchrotron radiation (beamline B2, HASYLAB at DESY, Hamburg, Germany) [27]. The diffraction experiments were performed in Debye-Scherrer capillary geometry with the samples filled in quartz capillaries using an on-site readable image plate detector OBI [28]. The wavelength of 0.68807 Å was calibrated using the reflection positions of a LaB_6 reference material (NIST SRM660a). The typical full-width at half-maximum (FWHM) of reflections obtained in this geometry was 0.06–0.08° for the reference material and 0.2-0.23° for the sample. A STOE furnace was used for *in situ* high temperature diffraction experiments. In order to estimate high temperature behavior of the nanocrystalline $La_{0.6}Ca_{0.4}Mn_{0.8}Fe_{0.2}O_{3\pm\delta}$, patterns were initially taken from room temperature to 1173 K in steps of 100 K (2 minutes for temperature stabilization and around 12 minutes for measuring the diffraction pattern). For all Rietveld refinements, the program package FullProf [29] was used. For all refinements against powder data, the scale factor, sample shift, cell dimensions, atomic coordinates, isotropic atomic displacement parameters and profile parameters were refined. Isotropic displacement parameters of oxygen were constrained so that $B_{O1}=B_{O2}$.

Scanning electron microscopy (SEM) and energy-dispersive X-ray spectroscopy (EDX) were performed in a Zeiss DMS 982 Gemini with the Noran Voyager EDX system.

The analysis of specific surface areas was carried out by means of physisorption measurements in a Sorptomatic 1990 and evaluated after Brunauer, Emmett and Teller (BET). The specific surface areas were calculated in the pressure range $0.05 \leq p/p_0 \leq 0.25$.

3 Results and Discussion

3.1 XRD

Fig. 1 shows X-ray powder diffraction patterns of the nanopowders synthesized in comparison with the LCMN82 bulkmaterial (**1**). Main features of the XRD patterns of the nanocrystalline powders studied in this work resemble well the bulk materials indicating perovskite structure of the materials synthesized. Besides, detectable amounts of parasitic phases, indicated by asterisks in Fig. 1, were detected in some samples. Compared to the XRD patterns of the bulkmaterials, the reflections of the perovskite phases in the nanomaterials synthesized are considerably broadened due to nanoscale particle sizes.

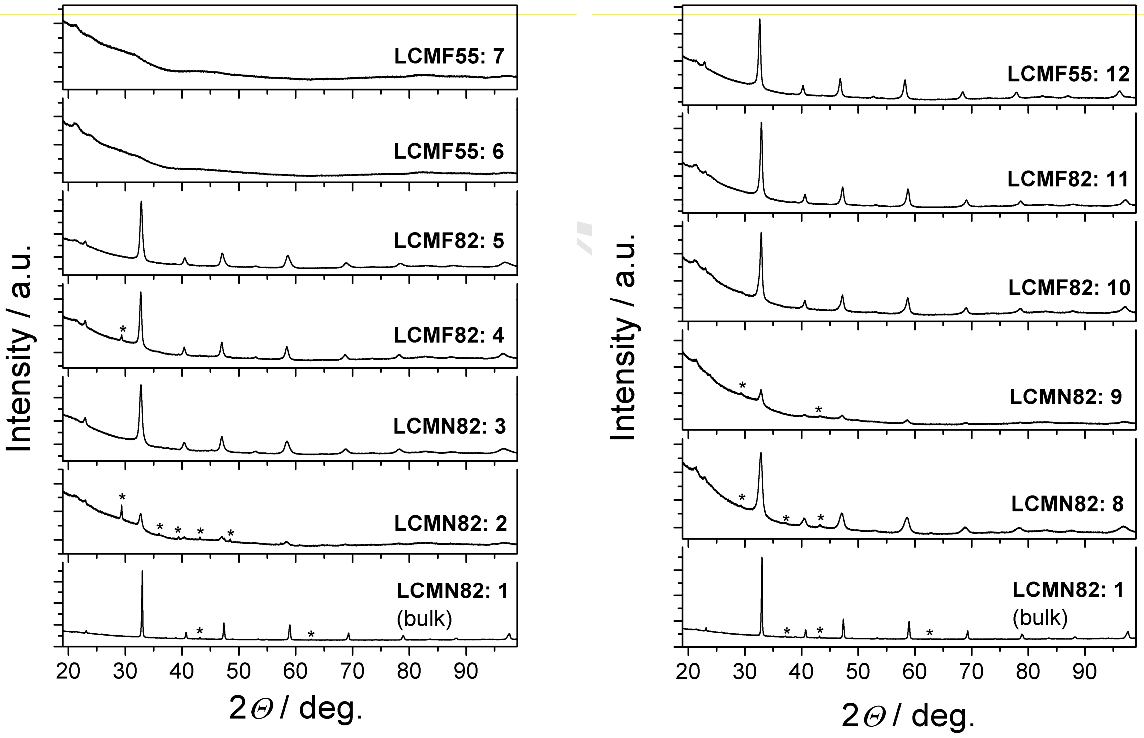

Fig. 1: XRD patterns of selected powders from the precipitation method (left panel) and the PVA/sucrose method (right panel): **LCMN82: 1** (bulkmaterial), **2** (500°C/5h), **3** (600°C/3h), **8** (600°C/3h), **9** (500°C/5h); **LCMF82: 4** (500°C/5h), **5** (600°C/3h), **10** (600°C/30min), **11** (600°C/3h); **LCMF55: 6** (700°C/3h), **7** (600°C/3h), **12** (600°C/3h). The values in brackets depict calcination temperature and time. Asterisks * indicate parasitic non-perovskite phases.

As it was reported in [30, 31], LCMN82 and LCMF82 bulkmaterials obtained by solid state technique adopt orthorhombic perovskite structure isotypic with $GdFeO_3$. The suggested structure of these materials was clearly proved by full profile Rietveld refinement performed by means of WinCSD program package [26]. As an example, the top panel of Fig. 2 demonstrates the graphical results of the Rietveld refinement of LCMN82 bulkmaterial performed in space group *Pnma*. All features of the experimental diffraction pattern are well fitted with the modeled pattern. As it was mentioned in [30], the $La_{0.6}Ca_{0.4}Mn_{1-x}Ni_xO_{3\pm\delta}$ samples obtained by solid state route contain some amount of (Ni,Mn)O impurities. Simultaneous two-phase full profile Rietveld refinement performed in the present study clearly proves the presence of 2.2(6) wt. % of NiO-based phase in the LCMN82 bulkmaterial sample (Fig. 2, inset on the top panel). Obtained structural parameters of the $La_{0.6}Ca_{0.4}Mn_{0.8}Ni_{0.2}O_{3\pm\delta}$ perovskite structure and corresponding residuals are presented in Table 1.

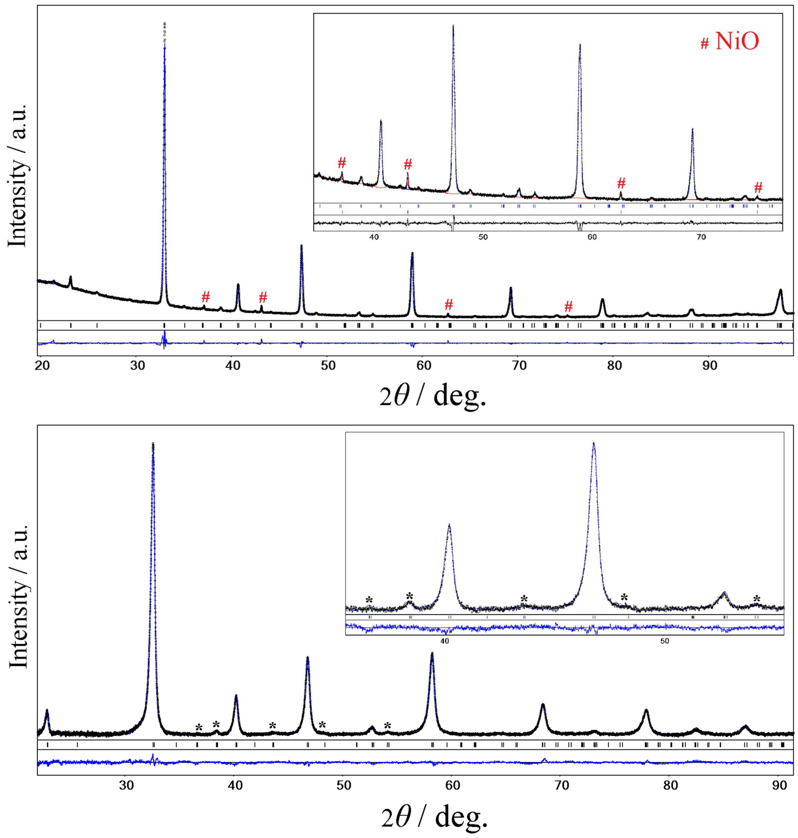

Fig. 2: Graphical results of the Rietveld refinement of the bulk $La_{0.6}Ca_{0.4}Mn_{0.8}Ni_{0.2}O_{3\pm\delta}$ (LCMN82-**1**) and nanocrystalline $La_{0.75}Ca_{0.25}Mn_{0.5}Fe_{0.5}O_{3\pm\delta}$ (LCMF55 (**12**)) structures (top and bottom panels, respectively). Experimental XRD patterns (black dots) are shown in comparison with the calculated patterns (blue lines). The difference between measured and calculated profiles is shown as curves below the diagrams. Short vertical bars indicate the positions of diffraction maxima in space group *Pbnm*. The inset on the top panel illustrates the two-phase Rietveld refinement showing presence of the NiO minority phase (red lines) in the LCMN82 (**1**) sample. Asterisks (*) on the bottom panel indicate weak superstructure reflections, which cannot by fitted in the cubic perovskite structure model.

Phase composition and crystal structure of the synthesized materials (except for the amorphous LCMF55 (**6 and 7**) samples) were confirmed by full profile Rietveld refinement. Graphical results of Rietveld refinement, proving *Pnma* orthorhombic structure of the nanocrystalline LCMF55 (**12**) sample with the nominal composition $La_{0.75}Ca_{0.25}Mn_{0.5}Fe_{0.5}O_{3\pm\delta}$ are presented on the bottom panel of Fig. 2. Despite the superstructure reflections indicating orthorhombic *Pnma* symmetry are very weak they are clearly detectable on the XRD pattern (Note, that the reflections marked with asterisks in Fig. 2 cannot be fitted in the cubic perovskite structure model.). Refined structural parameters of nanocrystalline $La_{0.75}Ca_{0.25}Mn_{0.5}Fe_{0.5}O_{3\pm\delta}$ sample are presented in Table 1.

Table 1: Crystallographic data for the bulk $La_{0.6}Ca_{0.4}Mn_{0.8}Ni_{0.2}O_{3\pm\delta}$ (LCMN82, **1**) and nanocrystalline $La_{0.75}Ca_{0.25}Mn_{0.5}Fe_{0.5}O_{3\pm\delta}$ (LCMF55, **12**) materials (space group *Pnma*, $Z = 4$)

Lattice parameters / Å and residuals	Atoms, sites	*x/a*	*y/b*	*z/c*	$B_{iso/eq}$ / Å^2
$La_{0.6}Ca_{0.4}Mn_{0.8}Ni_{0.2}O_{3\pm\delta}$ bulkmaterial (LCMN82, **1**)					
$a = 5.4154(1)$	La/Ca*, 4*c*	0.0181(2)	1/4	0.0032(4)	0.95(2)
$b = 7.6536(2)$	Mn/Ni**, 4*b*	0	0	1/2	0.63(2)
$c = 5.4342(1)$	O1, 4*c*	0.4883(13)	1/4	0.0677(14)	1.1(2)
R_I=0.044, R_P=0.086	O2, 8*d*	0.2869(14)	0.0151(9)	0.7200(15)	1.43(11)
* 0.606(3) La + 0.394(3) Ca; ** 0.91(6) Mn + 0.09(6) Ni					
Nanocrystalline $La_{0.75}Ca_{0.25}Mn_{0.5}Fe_{0.5}O_{3\pm\delta}$ (LCMF55, **12**)					
$a = 5.4834(7)$	La/Ca$^{\#}$, 4*c*	0.0113(3)	1/4	0.0074(4)	1.11(2)
$b = 7.7613(9)$	Mn/Fe$^{\#\#}$, 4*b*	0	0	1/2	0.50(3)
$c = 5.4690(9)$	O1, 4*c*	0.481(2)	1/4	0.007(4)	1.07(8)
R_I=0.060, R_P=0.102	O2, 8*d*	0.292(3)	0.0470(8)	0.706(2)	1.07(8)
$^{\#}$ 0.75 La + 0.25 Ca; $^{\#\#}$ 0.50 Mn + 0.50 Fe					

Choosing of the *Pnma* structural model for the structure refinement was corroborated by (*i*) a similarity of XRD patterns of the nanocrystalline samples with the bulk materials having similar compositions and (*ii*) by analysis of numerous literature publications on the parent perovskite systems. According to the comprehensive structural investigations of the calcium substituted lanthanum manganites performed by X-ray synchrotron and neutron powder diffraction (see [32-34] and references herein) $La_{1-x}Ca_xMnO_{3-\delta}$ adopt orthorhombic

Pnma structure for $0.2 \leq x \leq 1$ and rhombohedral $R\bar{3}c$ structure for $x \leq 0.14$. A miscibility gap between these two perovskite structures exists in the $La_{1-x}Ca_xMnO_{3-\delta}$ systems. Similar structure behaviour is also typical for the parent $La_{1-x}Ca_xFeO_3$, $LaMn_{1-x}Ni_xO_{3-\delta}$ and $LaMn_{1-x}Fe_xO_{3-\delta}$ systems [35-37], where either orthorhombic or rhombohedral phases are formed, depending on substitution level and partial oxygen pressure. A peculiarity of the orthorhombic solid solutions formed in the above-mentioned systems is a lattice parameters crossover and appearance of dimensionally cubic (pseudo-cubic) lattices at certain compositions. No tetragonal or cubic phases were reported in these systems so far.

Examination of XRD patterns of some samples revealed detectable asymmetry of the main perovskite reflections, which may indicate possible presence of the secondary perovskite phase with similar lattice parameters. Indeed, simultaneous two-phase Rietveld refinement performed in space groups *Pnma* and $R\bar{3}c$ (Fig. 3) confirm co-existence of orthorhombic and rhombohedral perovskite phases in the LCMF82 (**10**) sample with nominal composition $La_{0.6}Ca_{0.4}Mn_{0.8}Fe_{0.2}O_{3\pm\delta}$. This finding is not unexpected, because a coexistence of two perovskite phases is rather typical feature for the parent $La_{1-x}Ca_xMnO_{3-\delta}$ system [32-34].

Refined structural parameters of the two perovskite phases in the sample are analyzed and presented in Table 2.

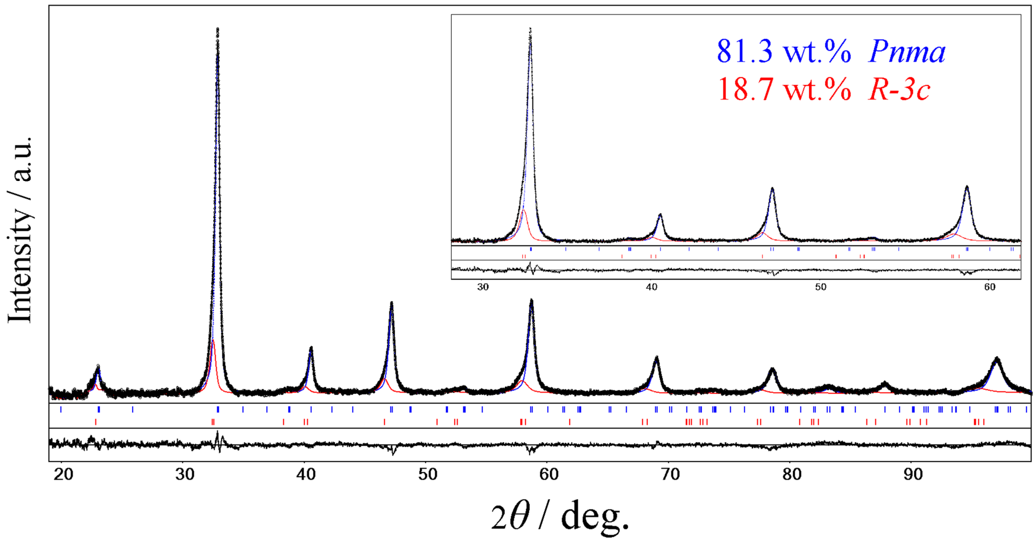

Fig. 3: Graphical results of two-phase Rietveld refinement showing coexistence of orthorhombic *Pnma* (blue) and rhombohedral $R\bar{3}c$ (red) phases in the LCMF82 (**10**) sample with nominal composition $La_{0.6}Ca_{0.4}Mn_{0.8}Fe_{0.2}O_{3\pm\delta}$. Short vertical bars indicate the positions of diffraction maxima of *Pnma* and $R\bar{3}c$ perovskite phases (upper and lower rows, respectively).

Table 2. Crystallographic data for *Pnma* and $R\bar{3}c$ perovskite phases in the LCMF82 (**10**) sample with nominal composition $La_{0.6}Ca_{0.4}Mn_{0.8}Fe_{0.2}O_{3\pm\delta}$.

Lattice parameters / Å	Atoms, sites	*x/a*	*y/b*	*z/c*	$B_{iso/eq}$ / Å^2
Pnma phase, 81.3(8) wt. %					
a = 5.435(3) *b* = 7.7092(8) *c* = 5.435(3)	La/Ca*, 4*c*	-0.0031(13)	1/4	0.0066(5)	0.94(1)
	Mn/Fe**, 4*b*	0	0	1/2	1.02(1)
	O1, 4*c*	0.513(7)		-0.021(4)	1.2(6)
	O2, 8*d*	0.256(4)	0.0542(11)	0.788(2)	1.2(6)
$R\bar{3}c$ phase, 18.7(8) wt. %					
a = 5.519(1) *c* = 13.419(6)	La/Ca*, 6*a*	0	0	1/4	0.82(1)
	Mn/Fe**, 6*b*	0	0	0	0.83(1)
	O, 18*e*	0.447(3)	0	1/4	2.0(8)
R_I(phase 1) = 0.027; R_I(phase 2) = 0.182; R_{WP} = 0.156					

* 0.60 La + 0.40 Ca; ** 0.80 Mn + 0.20 Fe

Figure 4 shows a polyhedral representation of the crystal structures of two perovskite phases coexisting in the LCMF82 (**10**) nanomaterial from PVA/sucrose. The structures are presented as a 3D framework of corner shared $(Mn/Fe)O_6$ octahedra with La/Ca species occupying holes between them. Both modifications of $La_{0.6}Ca_{0.4}Mn_{0.8}Fe_{0.2}O_{3\pm\delta}$ belong to the two most spread types of the distorted perovskite structures, namely orthorhombic $GdFeO_3$ and rhombohedral $NdAlO_3$ ones, which differ mainly with the character of cooperative tilting of the corner shared BO_6 octahera.

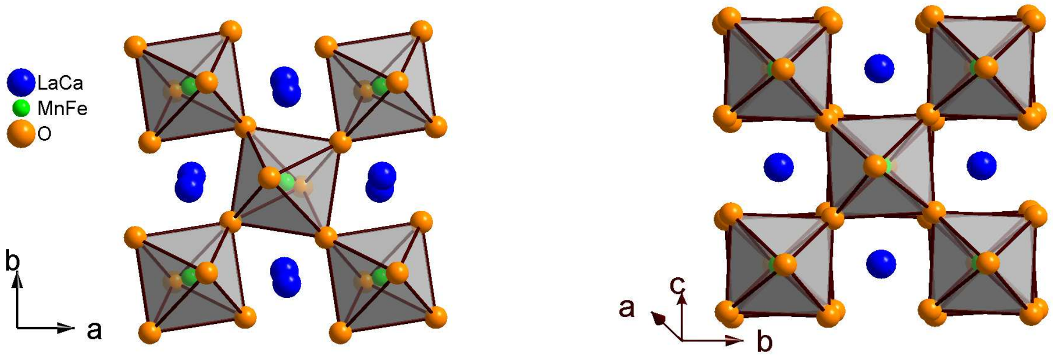

Fig. 4: Crystal structures of the orthorhombic *Pnma* (left) and rhombohedral $R\bar{3}c$ (right) perovskite structures of $La_{0.6}Ca_{0.4}Mn_{0.8}Fe_{0.2}O_{3\pm\delta}$ coexisting in LCMF82 nanomaterial.

Phase composition of the LCMN82, LCMF82 and LCMF55 nanomaterials and corresponding bulkmaterials as well as unit cell dimensions of the existing perovskite phases are presented in Table 3.

Table 3: Phase composition and unit cell dimensions of orthorhombic (*Or*) and rhombohedral (*Rh*) perovskite phases for selected samples; sample numbers follow the legend in Fig. 1.

Sample	Phase/s	Space group	a / Å	b / Å	c / Å	V / Å^3
LCMN82 bulkmaterial	per. + NiO	*Pnma*	5.4154(1)	7.6536(2)	5.4342(1)	225.24(1)
2	per. + $CaCO_3$			*not refined*		
3	*Or* per. + impurities	*Pnma*	5.474(1)	7.732(2)	5.431(1)	229.9(2)
8	per. + NiO	*Pnma*	5.438(5)	7.739(2)	5.440(4)	228.9(5)
9	*Or* per. + $CaCO_3$ (traces)	*Pnma*	5.430(3)	7.674(5)	5.490(3)	228.8(4)
LCMF82 bulkmaterial	*Or* per. + impurities	*Pnma*	5.4565(9)	7.725(1)	5.468(1)	230.5(1)
4	*Or* per. + $CaCO_3$	*Pnma*	5.4721(9)	7.735(1)	5.4348(8)	230.0(1)
5	*Or* + *Rh* per.	*Pnma*	5.383(3)	7.761(2)	5.386(3)	225.0(3)
		$R\bar{3}c$	5.4636(2)	-	13.2697(8)	343.05(4)
10	*Or* + *Rh* per.	*Pnma*	5.435(3)	7.7092(8)	5.435(3)	227.7(3)
		$R\bar{3}c$	5.519(1)	-	13.419(6)	353.9(3)
11	*Or* per.	*Pnma*	5.437(1)	7.698(2)	5.422(2)	226.9(2)
LCMF55 bulkmaterial	*Or* per. + impurities	*Pnma*	5.4870(9)	7.766(2)	5.490(1)	234.0(2)
6	amorphous					
7	amorphous					
12	*Or* per.	*Pnma*	5.4834(7)	7.7613(9)	5.4690(9)	232.75(10)

Some differences in the lattice parameters and unit cell volumes observed for the bulk- and nanomaterials with the same nominal composition can be explained by slightly varying compositions of the materials due to impurities since the initial weight of reactants was always stoichiometric. Another possible reason is the differing oxygen content frozen in the reaction product after cooling, especially since different preparation methods and temperatures were used.

In the precipitation method (**2, 4**), formation of LCMN82 and LCMF82 perovskite structures begins after calcination of the samples at 500°C for 5 hours. However, significant broadening of the diffraction maxima and a detectable amount of $CaCO_3$ calcite phase at the corresponding XRD patterns of LCMN82 (**2**) and LCMF82 (**4**) materials (Fig. 1, Table 3) indicate incomplete crystallization of the samples. After heat treatment at 600°C for 3 hours (**3**, **5**) the perovskite maxima in both samples become stronger and the $CaCO_3$ impurity phase disappears completely. In contrast, only traces of parasitic $CaCO_3$ phase could be detected in the PVA/sucrose synthesized LCMN82 (**9**) and LCMF82 (**11**). The formation of crystalline perovskite structures of $La_{0.6}Ca_{0.4}Mn_{0.8}Ni_{0.2}O_3$ and $La_{0.6}Ca_{0.4}Mn_{0.8}Fe_{0.2}O_3$ occurs after heat treatment at 500°C for 5 hours and 600°C for 30 min, respectively (items **9** and **10** in Fig.1 and Table 3).

For the LCMF55 materials obtained from the precipitation method no crystalline phases are formed after heat treatment of the samples at 600°C and 700°C (Fig. 1). From the XRD patterns of the LCMF55 specimens (**6, 7**) it is unclear whether perovskites or other oxides form amorphous phase when using this synthesis route. In contrast, the employment of the PVA/sucrose method leads to crystallization of $La_{0.75}Ca_{0.25}Mn_{0.5}Fe_{0.5}O_3$ perovskite phase in LCMF55 (**12**) material after calcination at 600 °C for 3 hours (Fig. 1, Table 3).

The results obtained show that wet chemistry methods can improve the synthesis of the iron manganites. The nanomaterials from precipitation method (LCMF82) and PVA/sucrose method (LCMF82, LCMF55) occur in pure perovskite phases compared to the bulkmaterials from solid state reaction which contain detectable amounts of undefined impurities.

3.2 EDX

EDX spectra were evaluated by comparing the ratios of elemental abundance (in atom %). The experimental ratios of the A ions (lanthanum to calcium) and the B ions (manganese to nickel or iron) agreed with ideal ratios calculated from the stoichiometry. The voltage of 20 kV was too high to evaluate the oxygen content properly. For this reason, reliable values regarding the oxygen contents of the powders are not available.

The powders from conventional solid-state reaction and the PVA/sucrose method form purely, while the powders from the precipitation method showed impurities of 4 to 8 atom percent of sodium ions, which are not detectable in the XRD. The sodium content could not be reduced by repeated washing of the powders with deionized water.

3.3 SEM after synthesis

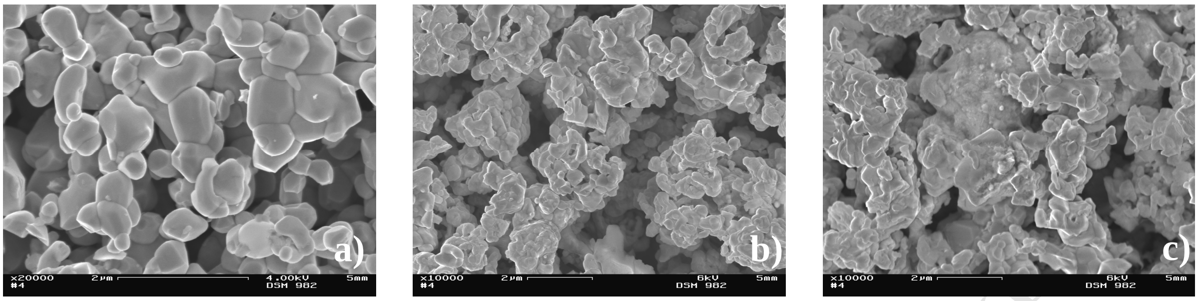

Fig. 5: SEM pictures of the bulkmaterials; a) LCMN82 (∅ (467±174) nm), b) LCMF82 (∅ (402±208) nm) and c) LCMF55 (no distinguishable particles).

Fig. 5 shows SEM pictures of powders from the solid state reaction which is described elsewhere [30]. This method yields the bulkmaterials with particle sizes of 467±174 nm (LCMN82) and 402±208 nm (LCMF82). The particles of the LCMF55 bulkmaterial cannot be distinguished, although the morphologies of both the iron manganites are similar and show agglomerates with diameters of about 2 µm. Only the agglomerates of LCMF82 are composed of smaller grains. In contrast, the LCMN82 bulkmaterial contains clearly defined particles. The precipitation method produces nanoparticles of the materials LCMN82 and LCMF82.

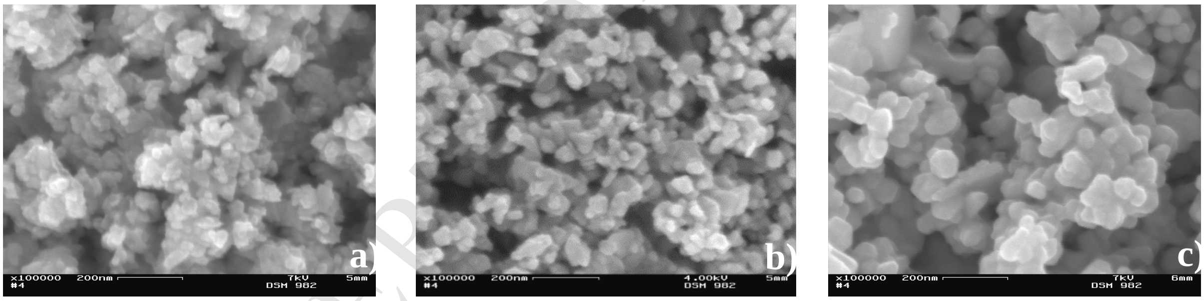

Fig. 6: SEM pictures of the LCMN82 nanomaterials from the precipitation method after calcination at different temperatures; a) 500°C (amorphous), b) 600°C (∅ (45±14) nm) and c) 700°C (∅ (65±15) nm).

Table 4: Precipitation method: Comparison of the particle sizes obtained from the evaluation of the SEM pictures and calculation from the physisorption measurements; n.m. …. no measurement, n.p. … no particles.

Material	Calcination conditions	Particle sizes and specific surface areas from physisorption	Particle sizes from SEM / nm
LCMN82	500°C, 5 hours	n.m.	n.p.
	600°C, 3 hours	56 nm (18 m^2/g)	45 ± 14
	700°C, 3 hours	94 nm (11 m^2/g)	65 ± 15
LCMF82	500°C, 5 hours	25 nm (42 m^2/g)	n.p.
	600°C, 3 hours	85 nm (12 m^2/g)	74 ± 22
	700°C, 3 hours	104 nm (10 m^2/g)	93 ± 24
LCMF55	500°C, 5 hours	n.m.	n.p.
	600°C, 3 hours	(168 m^2/g)	n.p.
	700°C, 3 hours	(251 m^2/g)	n.p.

Table 5: PVA/sucrose method: Comparison of the particle sizes obtained from the evaluation of the SEM pictures and calculation from the physisorption measurements; materials prepared at 600°C for 3 hours if not noted differently; n.p. … no particles.

Material	Specification	Particle sizes and specific surface areas from physisorption	Particle sizes from SEM / nm
LCMN82	mix. 1, PVA 145000	30 nm (33 m^2/g)	35 ± 6
	mix. 1, PVA 60000	48 nm (21 m^2/g)	43 ± 9
	mix. 2, PVA 60000	56 nm (18 m^2/g)	48 ± 20
LCMF82	mix. 2, PVA 60000	31 nm (33 m^2/g)	n.p.
	mix. 2, PVA 60000 600°C, 30 min	69 nm (15 m^2/g)	n.p.
LCMF55	mix. 2, PVA 145000	47 nm (22 m^2/g)	n.p.
	mix. 2, PVA 60000	86 nm (12 m^2/g)	n.p.

The enlargement of nanoparticles with increasing calcination temperature is pictured in Fig. 6 for the example of LCMN82. Since the material is amorphous after calcination at 500°C, particles cannot be distinguished and measured (Fig. 6 a). At 600°C and 700°C, particles are formed with sizes of 45±14 nm and 65±15 nm (Fig. 6 b, c and Table 4), respectively. The

LCMF82 particles form in the same morphology as the LCMN82 particles although they are larger with 74±22 nm and 93±24 nm at 600°C and 700°C, respectively. Expressed in percent, the distribution of particle sizes is slightly smaller for the LCMN82 nanomaterials compared to the bulkmaterial (the standard deviation equates 37% of the average value for the bulkmaterial while it is 31% (600°C) and 23% (700°C) for the nanomaterial). The distribution of particle sizes is much smaller for the LCMF82 nanomaterials (51% (bulkmaterial) compared to 30% (600°C) and 26% (700°C) for the nanomaterial). Also, compared to the bulkmaterial the LCMF82 nanomaterials show the formation of distinguishable particles, and thus forming a more defined morphology, which is advantageous beyond the purpose of this work for the optimization and interpretation of surface reactions such as catalysis or sensing (e.g. analysis of active sites for oxygen adsorption [40]).

Since the LCMF55 materials from the precipitation method are amorphous after different calcination temperatures (see XRD lines **6** and **7** in Fig. 1), the SEM pictures do not show any particles.

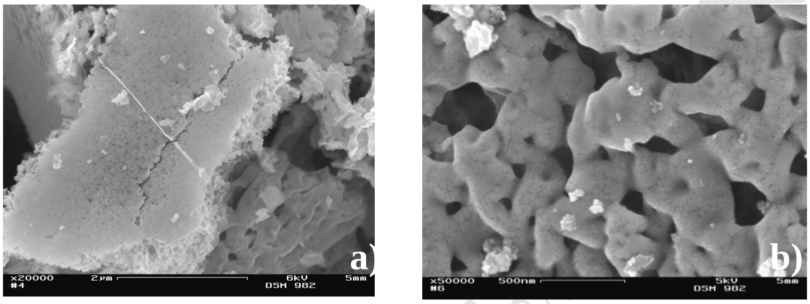

Fig. 7: SEM pictures of typical morphologies of powders from the PVA/sucrose method.

The materials from the PVA/sucrose method show a porous, network-like morphology. Figs. 7 a and b picture examples of different forms of this morphology. The network contains an additional porosity (Fig. 7 b).

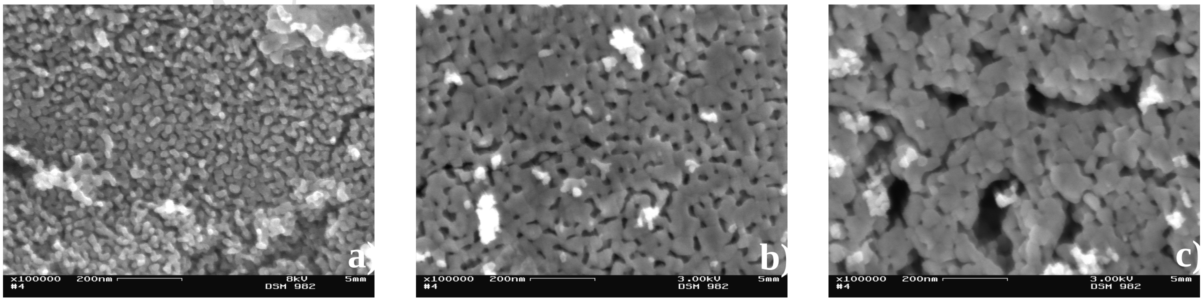

Fig. 8: SEM pictures of different positions on the same sample (LCMN82 from PVA/sucrose method (calcined 600°C/3h, mix 2, PVA 145000); a) ∅ 25 nm, b) ∅ 52 nm and c) ∅ 43 nm.

Figs. 8 a, b and c compare different positions in the same LCMN82 sample at high resolution (100000 times). The particles, which are hard to distinguish, range in particle size from 25 nm to 52 nm. This is an extraordinary difference which is based on the matrix-based preparation method. Obviously, the PVA/sucrose matrix and precursor do not form consistently over the whole sample, due to the irregular foaming process. Thus, the calcined nanomaterial, which is an imprint of the precursor, shows different morphologies in the same sample. Additionally, the LCMF82 and the LCMF55 nanomaterials do not form any distinguishable particles (see also Table 5). For characterization of the nanomaterials, it would be better to compare specific surface areas rather than particle sizes (see section 3.7), since they differ strongly in the same sample and are not accessible for some samples.

3.4 *SEM after temperature treatment*

For this study, powder samples of LCMN82, LCMF82 and LCMF55 as received after synthesis (both precipitation and PVA/sucrose method) were pressed to bars and sintered at 600°C and 800°C for 17 hours, respectively in order to compare SEM images regarding the change of particle sizes.

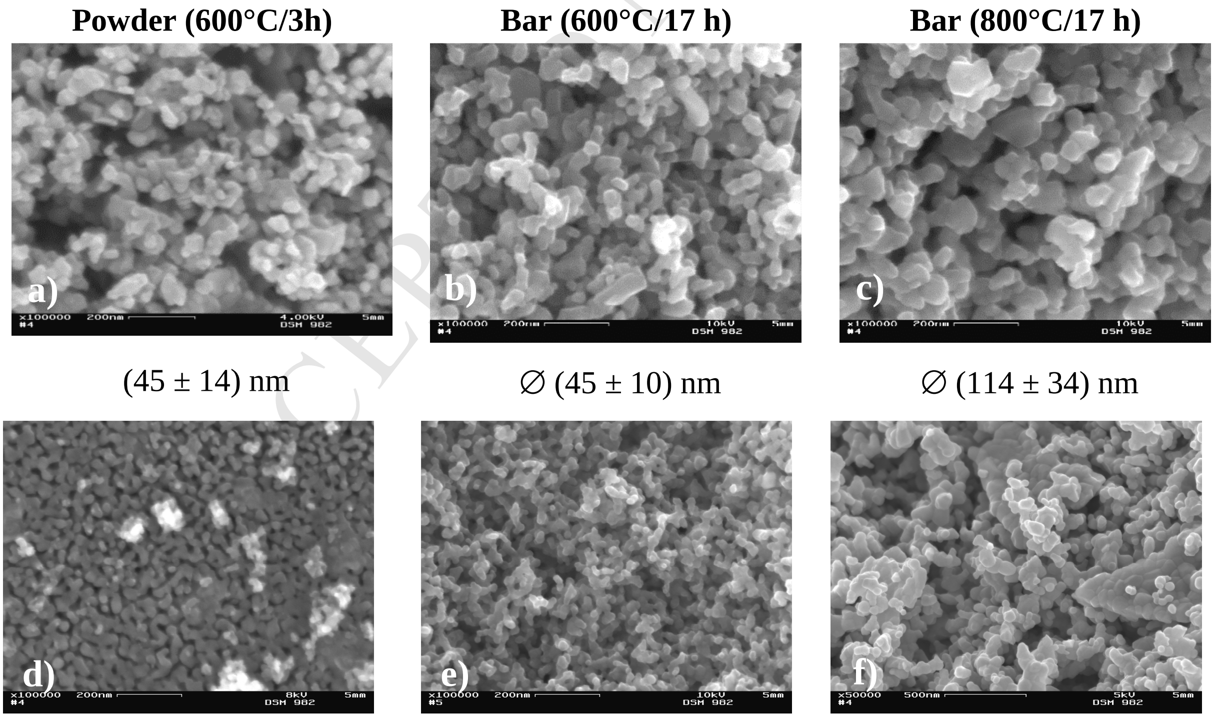

Powder (600°C/3h) **Bar (600°C/17 h)** **Bar (800°C/17 h)**

(45 ± 14) nm ∅ (45 ± 10) nm ∅ (114 ± 34) nm

∅ (35 ± 6) nm ∅ (36 ± 10) nm ∅ (86 ± 35) nm

Fig. 9: SEM pictures of the LCMN82 nanomaterials from the precipitation method (a, b, c) and the PVA/sucrose method (mix 1, PVA 145000) (d, e, f) before and after heat treatment.

Fig. 9 shows SEM pictures from LCMN82 samples received from precipitation synthesis (calcined 600°C/3h) and PVA/sucrose method (calcined 600°C/3h, mix 1, PVA 145000) before and after heat treatment at 600°C and 800°C. For both methods the particle sizes do not change after heat treatment at 600°C for 17 hours. In contrast, the change of particle sizes when heating the samples at 800°C for 17 hours due to particle agglomeration is significant. We found the same results for the LCMF82 and LCMF55 samples.

However, since the standard deviations are huge for all samples, we cannot finally decide whether agglomeration occurs regarding the Figs. 9 a and b as well as Figs. 9 c and d. We also have to take the results from Fig. 8 into account where we showed that the morphology and particle sizes differ significantly, especially for the materials from PVA/sucrose method. This decision is important because we aim for the usage of these materials in intermediate temperature applications around 500 to 600°C. Hence, we performed a study of particle size development *in situ* with another method, the temperature dependend XRD. Since this method also covers information about the whole sample volume instead of just small areas of the sample, overall information on particle sizes can be provided. The results are presented in the next section.

3.5 Microstructural features: analysis of temperature dependent line broadening in XRD

For possible applications in intermediate or high temperature devices such as SOFC or mixed potential sensors, the tendency to sintering at temperatures above 500°C has to be excluded. Hence, we investigated the temperature dependence of the microstructure using XRD in order to find out whether agglomeration occurs during heating.

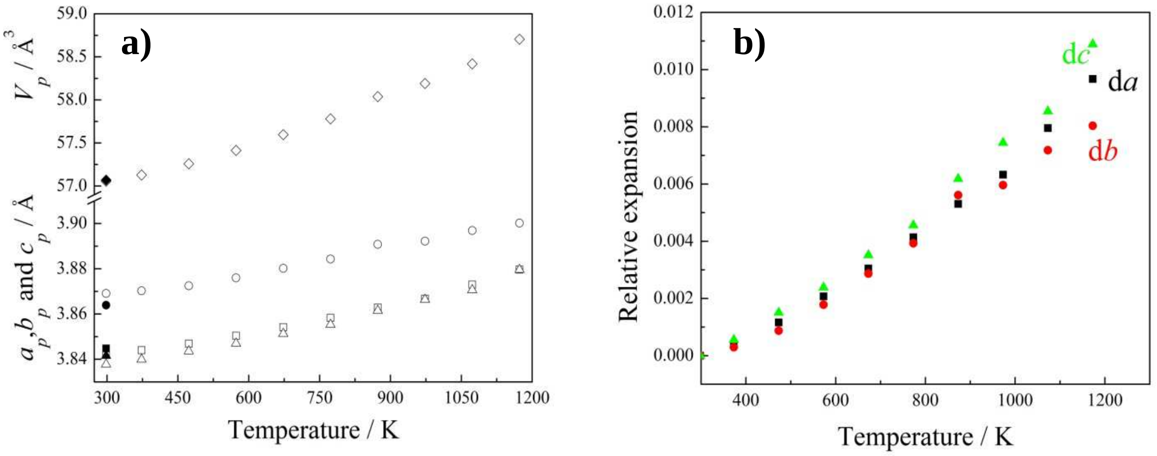

Fig. 10: Temperature dependence of a) normalized lattice parameters and b) relative lattice expansion of the LCMF82 nanomaterial from PVA/sucrose method; legend to a) diamonds

$V_p=V/4$; squares $a_p=a/2^{0.5}$, circles $b_p=b/2^{0.5}$ and triangles $c_p=c/2$. Filled symbols correspond to cell dimensions measured at room temperature again after high temperature measurements.

Temperature dependency of the lattice parameters is presented in Fig. 10 a. No phase transitions were detected up to the highest temperature. The relative expansion was calculated as $dl = \frac{l - l(293K)}{l(293K)}$, where l corresponds to the a, b or c lattice parameters. Slight anisotropy of thermal expansion might be seen in Fig. 10 b. Axes a and c expand more than axis b with relative expansions of around 1.0%, 1.1% and 0.8% at 1173 K, respectively.

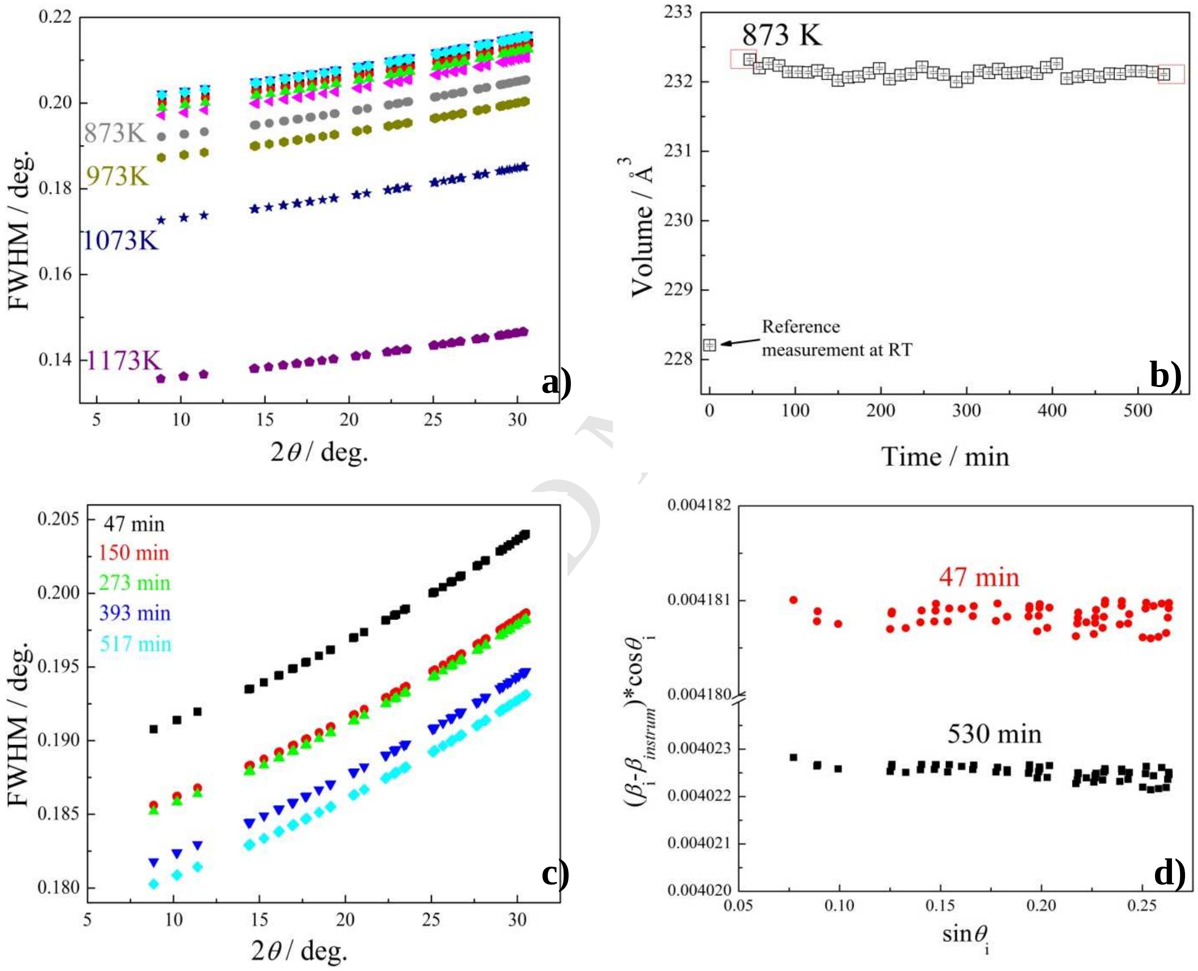

Fig. 11: Analysis of temperature dependent diffraction line broadening of the LCMF82 nanomaterial from PVA/sucrose method; a) Temperature dependent behavior of FWHMs of selected Bragg reflections vs. 2θ, b) Volume *vs.* time dependency at 873 K indicating stability of the sample during kinetic studies, c) FWHM *vs.* 2θ dependencies at different time points at 873 K and d) Williamson-Hall plots which illustrate temperature induced changes in the microstructure of nanocrystalline LCMF82.

Pronounced decrease of full-width at half-maxima (FWHM) of the diffraction lines was observed during high temperature diffraction at temperatures starting from 873 K (Fig. 11 a). Diffraction line broadening arises usually because of deviations from the ideal crystallinity, such as finite crystallite size and strain. In the particular case of nanocrystalline LCMF82, the temperature dependent decrease of FWHM corresponds very probably to temperature dependent agglomeration of nanoparticles. In order to confirm this assumption, we performed time-resolved powder diffraction investigation of line broadening in the scale of minutes. Here, we should also mention that no changes in broadening at temperature increase were observed for the LCMF82 bulkmaterial. A sample of LCMF82 nanopowder from the PVA/sucrose method was filled into a capillary, initially measured at ambient conditions and heated up to 873 K (temperature at which visible decrease of FWHM starts in Fig. 11a). 41 patterns were collected for 11 and 14 minutes duration per pattern at a constant temperature of 873 K. Fig. 11 b represents the independency of lattice volume on time at 873 K, indicating sample stability during diffraction experiments, whereas Fig. 11 c shows changes in FWHM vs. 2θ on time. The changes in FWHM on time at constant temperature are less pronounced comparable to changes in FWHM on temperature (Figs. 11 a and 11 c). Therefore, in order to “detect” possible agglomeration, we precisely analyzed peak broadening just for the first and last patterns measured at 873 K (these points are highlighted in Fig. 11 b). The simplest way to distinguish between “size” and “strain” is the analysis of the Williamson-Hall plot which allows separation of “size” and “strain” effects in the line broadening. For that, we have to describe refinements of the profile in detail. Pseudo-Voigt function was used for profile description (profile number 7 in FullProf), which is a combination of Gaussian and Lorentzian. Gaussian ($FWHM_G$) and Lorentzian ($FWHM_L$) components are calculated as

$$FWHM_G = (U + D_{ST}^2) \cdot \tan^2\theta + V \cdot \tan\theta + W + \frac{I_G}{\cos^2\theta} \quad \text{and}$$

$$FWHM_L = X \cdot \tan\theta + \frac{Y + F(S_z)}{\cos\theta},$$

where θ is the diffraction angle and U, V, W, I_G, D_{ST}, $F(S_z)$, X and Y are profile parameters (for their meaning see [29]). An analysis of instrumental broadening, which has to be subtracted from the profiles, was estimated by refinements of profile parameters of the LaB_6 reference material (the reference is assumed to be free from stress/size effects). Reasonable results were obtained by setting of I_G, D_{ST} and $F(S_z)$ to zero, so that the instrument resolution function is well described with non-zero values of U, V, W, X and Y. Thereafter, we implemented the instrument resolution function for further profile analysis. It was enough to fix the U, V, W and X parameters at values obtained for LaB_6 and refine just Y for correct profile description of nanocrystalline LCMF82. This means that the Gaussian part of the profile could be attributed only to instrumental effects and is negligible, whereas the Lorentzian part of the profile corresponds to microstructural and instrumental effects. Further analysis requires recalculation of the integral breadth β which is related to the Lorentzian profile as $\beta = \left(\frac{\pi}{2}\right) \cdot FWHM_L$ as well as introducing the expression for the Lorentzian Williamson–Hall plot (see for example [39]):

$$(\beta_i - \beta_{instrum})\cos\theta_i = \frac{\lambda}{D_v} + 4\varepsilon \cdot \sin\theta_i,$$

where β_i is the integral breadth (in radians) of the *i*th Bragg reflection positioned at $2\theta_i$, λ is the wavelength, D_v and ε are crystallite size and micro-strain. Therefore, D_v and ε can easily be calculated from intersection and slope, respectively, of the line in $(\beta_i\text{-}\beta_{instrum})\cos\theta_i$ vs. $\sin\theta_i$ dependency. Such dependencies for end-patterns (highlighted in Fig. 11 b) are presented in Fig. 11 d and no slopes are evident. This means zero contribution of micro-strains to the profiles of LCMF82. Crystallite sizes, calculated for the diffraction patterns measured 47 and 530 minutes after the experiment started at 873 K, are 164 Å and 171 Å, respectively. So, we detected undoubtedly agglomeration of nanoparticles at 873 K. However, we should mention that our analysis is rather qualitative because of large uncertainties of powder diffraction in comparison to other methods (see for example [38, 39] and references therein). We would propose therefore to introduce the relative value calculated as

$$100\% \cdot \frac{D_v(530min) - D_v(47min)}{D_v(47min)},$$

which shows the increase of particles compared to the initial state in %. Thus, $100\% \cdot {(171 - 164)}/{164} = 4.3\%$, which means that particles grow slowly at 600°C, resulting in 4.3% bigger particles after 8 hours. This small increase of the particle size makes the material a possible candidate for studies on applications in the intermediate temperature range.

The materials from precipitation synthesis cannot be studied with this method because the embedded sodium ions would corrode the quartz capillary during heat treatment.

3.6 Physisorption measurements (BET)

Table 4 shows the specific surface areas of the powders from the precipitation method. The surface areas of LCMN82 and LCMF82 decrease with increasing calcination temperature as expected. They vary from 10 m^2/g to 42 m^2/g and agree with results described in the literature for perovskite-type iron manganites of different compositions (20 m^2/g to 35 m^2/g) [21, 41]. The specific surface areas of the LCMF55 materials are unusual high with 168 m^2/g and 251 m^2/g. As shown in the XRD in Fig. 1 a (patterns **6** and **7**), these materials are amorphous and the specific surface areas are not comparable to the values of crystalline materials. The particle sizes in Table 2 are calculated from the physisorption measurements using a formula described by Rouquerol [42]:

$$d = \frac{6}{\rho \cdot S_g},$$

where d is the particle size, ρ is the theoretical density and S_g is the specific surface area. The values from this equation (theoretical) are compared with the particle sizes determined from the SEM pictures (experimental) which were measured on printouts with a ruler. The theoretical and experimental values are in agreement with each other (Table 4). This shows that the equation is applicable for the materials.

The materials from the PVA/sucrose method show slightly higher specific surface areas than the materials from the precipitation method after calcination at 600°C after 3 hours (Table 5). The LCMN82 materials show a dependence of the mixture and the number of monomer units of PVA. Mixture 1 with PVA 145000 yields the smallest particle sizes and the highest specific surface area. The reaction with mixture 1 using PVA 60000 leads to a lower specific surface area which is still higher than the surface area of the material from mixture 2. Thus, using PVA with a higher molar mass as well as low metal ion content in the reaction mixture leads to higher specific surface areas. The calculated and measured particle sizes of the LCMN82 nanomaterial agree with each other (Table 5).

In agreement with the results for LCMN82, using PVA 145000 for preparing the LCMF55 material yields a specific surface area which is twice as high as the one using PVA 60000. Table 5 also shows that the specific surface area of the LCMF82 nanomaterial calcined at 600°C for 30 minutes is about twice as high as the surface area of the material calcined at 600°C for 3 hours. This can be explained with the proceeding sintering process which is not finished after 30 minutes. This result is important considering the temperature of a possible application in sensing, catalysis or SOFC. If this temperature is equal to or higher than 600°C, the material has to be sintered for a longer time and at higher temperatures accepting smaller specific surface areas.

Summarizing the physisorption measurements, using PVA 145000 and mixture 1 in further experiments might lead to optimizing the reaction (also considering temperature and temperature ramp) in yielding higher specific surface areas. The curve progression of the desorption isotherms compared to the adsorption isotherms shows hysteresis which indicates mesoporosity (not pictured).

4 Conclusions

LCMN82, LCMF82 and LCMF55 nanomaterials can be prepared by precipitation synthesis and the PVA/sucrose method. The materials are crystalline after calcination at 600°C. Nanocrystalline LCMF55 can only be prepared by the PVA/sucrose method. The precipitation synthesis yields materials with distinguishable nanoparticles with diameters between 45 nm and 93 nm whereas the PVA/sucrose method results in a mesoporous network-like morphology which is better characterized by specific surface area. The nanomaterials show specific surface areas between 10 m^2/g and 42 m^2/g which are comparable to similar materials described in the literature. Long term XRD measurements at 600°C show a slight growth of the nanoparticles from the PVA/sucrose method. Since the materials from the PVA/sucrose method occur without impurities and with higher surface areas, they are the better choice for a further use in electrochemical experiments because the measurements will not be disturbed by foreign ions and the measuring set-ups will not be damaged.

Chosen materials from this study will be used as electrode materials for electrochemical NO sensing and conductivity measurements. The results will be presented elsewhere.

Acknowledgement

D.F. would like to thank Dr. Horst Borrmann (Max Planck Institute for Chemical Physics of Solids, Dresden, Germany) for carrying out the XRD measurements on the Huber Image Plate camera and Dr. K. Räuchle (Institute of Industrial Chemistry, Technische Universität Dresden, Germany) for the physisorption measurements.

Financial support by the DFG (Deutsche Forschungsgemeinschaft) graduate school project 1401/2 “Nano and Biotechniques for the Packaging of Electronic Systems” is gratefully acknowledged. L.V. acknowledges a partial support of the Ukrainian Ministry of Education and Sciences (Project “RZE”).

References

[1] C. Bergner, V. Vashook, S. Leoni, H. Langbein, $VNb_9O_{25-\delta}$ - Synthesis, electrical conducting behavior and density functional theory (DFT) calculation, J Solid State Chem 182 (2009) 2053-2060

[2] C. Chen, J. Cheng, S. Yu, L. Che, Z. Meng, Hydrothermal synthesis of perovskite bismuth ferrite crystallites, J Cryst Growth 291 (2006) 135-139

[3] S. Kang, B. S. Kwak, B.-H. Choi, S.-M. Park, M.J. Ji, M. Kang, Characteristics of nano-sized perovskite structured LaSrMn derived from hydrothermally synthesized amorphous LaSrMn oxide powder, J Ind Eng Chem (2014); http://dx.doi.org/10.1016/j.jiec.2014.01.022

[4] S. Fuentes, R.A. Zarate, E. Chavez, P. Muñoz, D. Díaz-Droguett, P. Leyton, Preparation of $SrTiO_3$ nanomaterial by sol-gel-hydrothermal method, J Mater Sci 45 (2010) 1448-1452

[5] Y. He, Y. Zhu, Solvothermal Synthesis of Sodium and Potassium Tantalate Perovskite Nanocubes, Chem Lett 33 (2004) 900-901

[6] Z. Fu, B.K. Moon, H.K.Yang, J.H. Jeong, Solvothermal Synthesis and Luminescent Properties of $BaTiO_3$:Pr^{3+} Nanocrystals, J Korean Phys Soc 51 (2007) 2036-2039

[7] J. Kirchnerova, C. Tofan, D. Klavna, Perovskites in environmental and related catalysis: Their potential and limitations, Recent Res Devel Solid State Ionics 2 (2004) 1-32

[8] T. Ahmad, K.V. Ramanujachary, S. E. Lofland, A.K. Ganguli, Reverse micellar synthesis and properties of nanocrystalline GMR materials ($LaMnO_3$, $La_{0.67}Sr_{0.33}MnO_3$ and $La_{0.67}Ca_{0.33}MnO_3$): Ramifications of size considerations, J Chem Sci 118 (2006) 513-518

[9] V. Uskoković, M. Drofenik, I. Ban, The characterization of nanosized nickel-zinc ferrites synthesized within reverse micelles of CTAB/1-hexanol/water microemulsion, J Magn Magn Mater 284 (2004) 294-302

[10] M. Schwickardi, T. Johann, W. Schmidt, F. Schüth, High-Surface-Area Oxides Obtained by an Activated Carbon Route, Chem Mater 14 (2002) 3913-3919

[11] S. Wohlrab, M. Weiss, H. Du, S. Kaskel, Synthesis of MNbO3 Nanoparticles (M = Li, Na, K), Chem Mater 18 (2006) 4227-4230

[12] M. Siemons, Th. Weirich, J. Mayer, U. Simon, Preparation of Nanosized Perovskite-type Oxides via Polyol Method, Z Anorg Allg Chem 630 (2004) 2083-2089

[13] S. Vasseur, E. Duguet, J. Portier, G. Goglio, S. Mornet, E. Hadová, K. Knížek, M. Maryško, P. Veverka, E. Pollert, Lanthanum manganese perovskite nanoparticles as possible in vivo mediators for magnetic hyperthermia, J Magn Magn Mater 302 (2006) 315-320

[14] A.B. Panda, A. Tarafdar, S. Sen, A. Pathak, P. Pramanik, Preparation of nanocrystalline

$SrBi_2Ta_2O_9$ powders using sucrose-PVA as the polymeric matrix, J Mater Sci 39 (2004) 3739-3744

[15] P. Pramanik, Chemical synthesis of nanosized oxides, B Mater Sci 19(6) (1996) 957-961

[16] L. Zhang, H. Qin, P. Song, J. Hu, M. Jiang, Electric properties and acetone-sensing characteristics of $La_{1-x}Pb_xFeO_3$ perovskite system, Mater Chem Phys 98 (2006) 358-362

[17] P. Song, H. Qin, L. Zhang, K. An, Z. Lin, J. Hu, M. Jiang, The structure, electrical and ethanol-sensing properties of $La_{1-x}Pb_xFeO_3$ perovskite ceramics with $x \leq 3$, Sens Actuat B 104 (2005) 312-316

[18] L. Zhang, J. Hu, P. Song, H. Qin, K. An, X. Wang, M. Jiang, CO-sensing properties of perovskite $La_{0.68}Pb_{0.32}FeO_3$ nano-materials, Sens Actuat B 119 (2006) 315-318

[19] J.W. Yoon, M.L. Grilli, E. Di Bartolomeo, R. Polini, E. Traversa, The NO_2 response of solid electrolyte sensors made using nano-sized $LaFeO_3$ electrodes, Sens Actuat B 76 (2001) 483-488

[20] E. Di Bartolomeo, N. Kaabbuathong, A. D'Epifanio, M.L. Grilli, E. Traversa, H. Aono, Y. Sadaoka, Nano-structured perovskite oxide electrodes for planar electrochemical sensors using tape casted YSZ layers, J Eur Ceram Soc 24 (2004) 1187-1190

[21] J.M. Serra, S. Uhlenbruck, W.A. Meulenberg, H.P. Buchkremer, D. Stöver, Nano-structuring of solid oxide fuel cells cathodes, Top Catal 40 (2006) 123-131

[22] A. Subramania, T. Saradha, S. Muzhumathi, Synthesis of nano-crystalline $(Ba_{0.5}Sr_{0.5})Co_{0.8}Fe_{0.2}O_{3-\delta}$ cathode material by a novel sol-gel thermolysis process for IT-SOFCs, J Power Sources 165 (2007) 728- 732

[23] V.V. Zyryanov, V.A. Sadykov, M.I. Ivanovskaya, J.M. Criado, S. Neophytides, Synthesis and Sintering of Ceramic Nanocomposites with High Mixed Conductivity, Sci Sinter 37 (2005) 45-54

[24] J. Zosel, D. Franke, K. Ahlborn, F. Gerlach, V. Vashook, U. Guth, Perovskite related electrode materials with enhanced NO sensitivity for mixed potential sensors, Solid State Ionics 179 (2008) 1628-1631

[25] D. Franke, J. Zosel, U. Guth, NO sensitivity of perovskite-type electrode materials $La_{0.6}Ca_{0.4}B'_{1-x}B''_xO_{3\pm\delta}$ (B' = Mn, Cr; B'' = Ni, Fe, Co; x = 0, 0.1, …, 0.6) in mixed potential sensors, Sensors and Actuators B 223 (2016) 723-729

[26] L.G Akselrud, P. Yu. Zavalij, Yu. Grin, V.K. Pecharsky, B. Baumgartner, E Woelfel, Use of the CSD Program Package for Structure Determination from Powder Data, Mater Sci Forum 133-136 (1993) 335-340

[27] M. Knapp, C. Baehtz, H. Ehrenberg and H. Fuess, The synchrotron powder diffractometer at beamline B2 at HASYLAB/DESY: status and capabilities, J Synchrotron Radiat 11 (2004) 328–334

[28] M. Knapp, V. Joco, C. Baehtz, H.H. Brecht, A. Berghaeuser, H. Ehrenberg, H. von Seggern and H. Fuess, Position-sensitive detector system OBI for High Resolution X-Ray Powder Diffraction using on-site readable image plates, Nucl Instrum Methods A 521 (2004) 565–570

[29] http://www.ill.eu/sites/fullprof/ (retrieved 2017-07-09)

[30] V. Vashook, D. Franke, J. Zosel, K. Ahlborn, L. Vasylechko, W. Fichtner, U. Guth, Transport properties of the double B mixed perovskite series $La_{0.6}Ca_{0.4}Mn_{1-x}Ni_xO_{3-\delta}$ with x=0-0.6, Solid State Ionics 179 (2008) 135-142

[31] V. Vashook, D. Franke, L. Vasylechko, J. Zosel, J. Rebello, K. Ahlborn, W. Fichtner, M. Schmidt, T.-L. Wen, U. Guth, Electrical conductivity and oxygen non-stoichiometry of the double B mixed perovskite series $La_{0.6}Ca_{0.4}Mn_{1-y}Me_yO_{3-\delta}$ with Me=Fe, Co, Ni and x=0-0.6, Solid State Ionics 179 (2008) 1101-1107

[32] P.G. Radaelli, M. Marezio, H.Y. Hwang, and S.-W. Cheong, Structural phase diagram of perovskite $A_{0.7}A'_{0.3}MnO_3$ (A = La, Pr; A' = Ca, Sr, Ba): a new *Imma* allotype, J Solid State Chem 122 (1996) 444-447

[33] P.M. Woodward, T. Vogt, D.E. Cox, A. Arulraj, C.N.R. Rao, P. Karen, and A.K. Cheetham, Influence of cation size on the structural features of $Ln_{1/2}A_{1/2}MnO_3$ perovskites at room temperature, Chem Mater 10 (1998) 3652-3665

[34] L. Rørmark, K. Wiik, S. Stølenand, T. Grande, Oxygen stoichiometry and structural properties of $La_{1-x}A_xMnO_{3\pm\delta}$ (A = Ca or Sr and $0 \le x \le 1$), J Mater Chem 12 (2002) 1058-1067

[35] M.-H. Hung, M.V. Madhava Rao, Dah-Shyang Tsai, Microstructures and electrical properties of calcium substituted $LaFeO_3$ as SOFC cathode, Materials Chem Phys 101 (2007) 297-302

[36] J. Blasco, M.C. Sánchez, J. Pérez-Cacho, J. García, G. Subías, J. Campo, Synthesis and structural study of $LaNi_{1-x}Mn_xO_{3+\delta}$ perovskites, J Phys Chem Solids 63 (2002) 781-792

[37] X.-D. Zhou and L. R. Pederson, Structural and magnetic properties of $LaMn_{1-x}Fe_xO_3$ (0<x<1.0), J Appl Phys 99 (2006) 08M918

[38] P. Karen, P.M. Woodward, Liquid-mix disorder in crystalline solids: $ScMnO_3$, J Solid State Chem 141 (1998) 78-88

[39] P. Scardi, M. Leoni, R. Delhez, Line broadening analysis using integral breadth methods:

a critical review, J Appl Cryst 37 (2004) 381-390

[40] L. Sun, H. Qin, E. Cao, M. Zhao, F. Gao, J. Hu, Gas-sensing properties of perovskite $La_{0.875}Ba_{0.125}FeO_3$ nanocrystalline powders, J Phys Chem Solids 72 (2011) 29-33

[41] K. Sahner, D. Schönauer, M. Matam, M. Post, R. Moos, Selectivity enhancement of p-type semiconducting hydrocarbon sensors - The use of sol-precipitated nano-powders, Sens Actuat B 130 (2008) 470-476

[42] F. Rouquerol, J. Rouquerol, K. Singh, Adsorption by Powders and Porous Solids (1999) Academic Press, London

Highlights

- We used precipitation and PVA/sucrose method.
- Perovskite-type nanomaterials were prepared.
- We found particle sizes between 33 nm and 93 nm.
- Agglomeration was interpreted using temperature dependent long term XRD and SEM.